



SN 2022jox: An Extraordinarily Ordinary Type II SN with Flash Spectroscopy

Jennifer E. Andrews¹ , Jeniveve Pearson² , Griffin Hosseinzadeh² , K. Azalee Bostroem² , Yize Dong (董一泽)³ , Manisha Shrestha² , Jacob E. Jencson⁴ , David J. Sand² , S. Valenti³ , Emily Hoang³ , Daryl Janzen⁵ , M. J. Lundquist⁶ , Nicolás Meza³ , Samuel Wyatt⁷ , Saurabh W. Jha⁸ , Chris Simpson¹ , Joseph Farah^{9,10} , Estefania Padilla Gonzalez^{9,10} , D. Andrew Howell^{9,10} , Curtis McCully^{9,10} , Megan Newsome^{9,10} , Craig Pellegrino^{9,10} , and Giacomo Terreran^{9,10}

¹ Gemini Observatory/NSF's NOIRLab, 670 N. A'ohoku Place, Hilo, HI 96720, USA

² Steward Observatory, University of Arizona, 933 North Cherry Avenue, Tucson, AZ 85721-0065, USA

³ Department of Physics and Astronomy, University of California, Davis, 1 Shields Avenue, Davis, CA 95616-5270, USA

⁴ Department of Physics and Astronomy, The Johns Hopkins University, 3400 North Charles Street, Baltimore, MD 21218, USA

⁵ Department of Physics & Engineering Physics, University of Saskatchewan, 116 Science Place, Saskatoon, SK, S7N 5E2, Canada

⁶ W.M. Keck Observatory, 65-1120 Mamalahoa Highway, Kamuela, HI 96743, USA

⁷ DIRAC Institute, Department of Astronomy, University of Washington, 3910 15th Avenue NE, Seattle, WA 98195, USA

⁸ Department of Physics and Astronomy, Rutgers, the State University of New Jersey, 136 Frelinghuysen Road, Piscataway, NJ 08854-8019, USA

⁹ Las Cumbres Observatory, 6740 Cortona Drive, Suite 102, Goleta, CA 93117-5575, USA

¹⁰ Department of Physics, University of California, Santa Barbara, Broida Hall, Santa Barbara, CA 93106-9530, USA

Received 2023 October 22; revised 2024 February 13; accepted 2024 February 14; published 2024 April 9

Abstract

We present high-cadence optical and ultraviolet (UV) observations of the Type II supernova (SN), SN 2022jox which exhibits early spectroscopic high-ionization flash features of H I, He II, C IV, and N IV that disappear within the first few days after explosion. SN 2022jox was discovered by the Distance Less Than 40 Mpc survey ~ 0.75 day after explosion with follow-up spectra and UV photometry obtained within minutes of discovery. The SN reached a peak brightness of $M_V \sim -17.3$ mag, and has an estimated ^{56}Ni mass of $0.04 M_\odot$, typical values for normal Type II SNe. The modeling of the early light curve and the strong flash signatures present in the optical spectra indicate interaction with circumstellar material (CSM) created from a progenitor with a mass-loss rate of $\dot{M} \sim 10^{-3} - 10^{-2} M_\odot \text{ yr}^{-1}$. There may also be some indication of late-time CSM interaction in the form of an emission line blueward of H α seen in spectra around 200 days. The mass-loss rate of SN 2022jox is much higher than the values typically associated with quiescent mass loss from red supergiants, the known progenitors of Type II SNe, but is comparable to inferred values from similar core-collapse SNe with flash features, suggesting an eruptive event or a superwind in the progenitor in the months or years before explosion.

Unified Astronomy Thesaurus concepts: Type II supernovae (1731); Circumstellar matter (241)

Supporting material: data behind figures

1. Introduction

Core-collapse supernovae (CCSNe) are the result of the deaths of the most massive stars ($> 8 M_\odot$). In particular, those stars exploding with a large fraction of their hydrogen envelope still intact are classified as Type II events (see Arcavi 2017, Branch & Wheeler 2017, and Gal-Yam 2017 for detailed reviews) and have been confirmed to come from red supergiant (RSG) progenitor stars via Hubble Space Telescope imaging (Smartt 2015; Van Dyk 2015). These supernovae (SNe) are often subdivided into Type IIP and Type IIL subclasses by optical light-curve behavior. Type IIP SNe show plateau features as the recombination front moves through the hydrogen envelope $\sim 2-3$ months after maximum, while Type IIL show an almost linear decline from peak, although as the sample size increases there is evidence of a continuous class of objects (Valenti et al. 2016; Hiramatsu et al. 2021).

Over the last decade, early spectroscopic observations of Type II SNe in the hours to days after explosion have revealed narrow, high-ionization emission (“flash”) features of elements

such as hydrogen, helium, carbon, oxygen, and nitrogen located in a dense and confined shell around the SN, which is a direct result of the mass loss from the progenitor (Gal-Yam et al. 2014; Groh et al. 2014; Davies & Dessart 2019). These lines often have Lorentzian profiles due to electron scattering, with wings extending out to $1500-2000 \text{ km s}^{-1}$, and can develop narrow P-Cygni absorption from any cool, dense material along the observer’s line of sight. The physical characteristics of the circumstellar material (CSM) such as the density, temperature, and composition determine the ionization species and line profiles seen, making early spectroscopy a powerful tool for understanding the transition between an evolved massive star and a SN.

These narrow flash features have only been observed in a handful of historical SNe (Niemela et al. 1985; Benetti et al. 1994; Leonard et al. 2000; Quimby et al. 2007), but with the recent advancements in SN searches and the rapid response of spectroscopic follow-up the numbers of objects showing fleeting narrow lines have grown substantially (see, e.g., Gal-Yam et al. 2014; Smith et al. 2015; Khazov et al. 2016; Yaron et al. 2017; Bullivant et al. 2018; Hosseinzadeh et al. 2018; Nakaoka et al. 2018; Bruch et al. 2021; Tartaglia et al. 2021; Jacobson-Galán et al. 2022; Terreran et al. 2022). In fact, Bruch et al. (2021) found that among their sample of Type II SNe, a third or more of CCSNe show these lines in the first few days



Original content from this work may be used under the terms of the [Creative Commons Attribution 4.0 licence](#). Any further distribution of this work must maintain attribution to the author(s) and the title of the work, journal citation and DOI.

after explosion. Rapid spectroscopic follow-up was essential in obtaining unprecedented data for the recent nearby Type II SN 2023ixf, including a high-cadence time series showing the evolution of the flash features, which will likely be used as a cornerstone of CCSN research for years to come. Comprehensive analysis of the early light curve and spectra of SN 2023ixf are discussed in Hosseinzadeh et al. (2023b), Bostroem et al. (2023), Smith et al. (2023), Jacobson-Galán et al. (2023), Hiramatsu et al. (2023), Zhang et al. (2023), and Li et al. (2023).

Enhanced mass loss in massive stars such as luminous blue variables (LBVs) or Wolf-Rayet (WR) stars occurs in the years before explosion (see Smith 2014 for a review), but was not necessarily expected in RSGs, where there is not yet a consensus on mass-loss rates. Whether using the canonical prescription from de Jager et al. (1988), which may already overestimate the mass-loss rates (Beasor et al. 2020), or the even higher mass-loss rates of Ekström et al. (2012), the luminosity would have to greatly exceed the Eddington limit to approach the quiescent mass-loss rates needed to create the CSM interaction seen at early times. This tension can be eased if periods of enhanced mass loss are considered for RSGs. These could be caused via wave-driven mass loss during late-stage nuclear burning (Quataert & Shiode 2012; Fuller 2017; Wu & Fuller 2021), turbulent convection in the core due to some dynamical instability (Smith & Arnett 2014), or even interaction with a companion as the binary fraction for massive stars is high (Sana et al. 2012). For normal Type II SNe, though, eruptive mass loss from the progenitor may be ruled out from observational surveys (e.g., Kochanek et al. 2017; Dong et al. 2023) unless these pre-SN eruptions are brief, faint, dusty, or some combination of all three; although, see Jacobson-Galán et al. (2022) for a possible exception. Interestingly, recent studies suggest that explosive mass-loss events should be expected in the months to years before core collapse in RSGs and are likely the main contributor to the elevated mass loss seen in Type II SNe (Davies et al. 2022).

Even though the number of known Type II SNe with flash spectroscopy has greatly increased, every new object added to the sample increases our understanding of CCSNe and massive star evolution. Within this boon of very early spectroscopy, we have uncovered objects with various time durations of narrow lines, differing species of lines, or even those without the traditional narrow flash ionization lines, but instead a broader, blueshifted feature, particularly around the N IV and N III lines at $\sim 4600 \text{ \AA}$. Explanations for this particular feature range from high-velocity H β (Pastorello et al. 2006), broad blueshifted He II (Quimby et al. 2007; Gal-Yam et al. 2011; Bullivant et al. 2018; Andrews et al. 2019), or a blend of several species such as N IV, N III, C III, O III, and He II (Dessart et al. 2017; Soumagnac et al. 2020; Bruch et al. 2021; Hosseinzadeh et al. 2022; Pearson et al. 2023; Shrestha et al. 2024). SN 2022jox, the object discussed in detail here, is a rare instance where we see an evolution from narrow emission lines to the broad feature in this wavelength range over the first few days after explosion, which allows us to fill in important information on the possible progenitors and pre-SN mass loss for these early and briefly interacting SNe.

In Section 2 of this paper, we outline the discovery and subsequent observations and data reduction. We discuss the photometric and bolometric evolution in Section 3. Section 4 details the spectroscopic evolution of the object. The

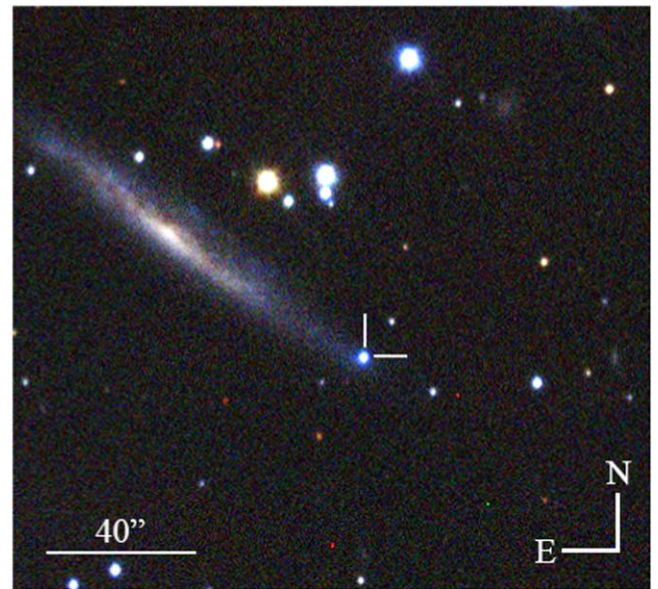


Figure 1. Composite *gri* Las Cumbres Observatory image of SN 2022jox taken on 2022 May 9.

implications of the observational data are laid out in Section 5. Finally, the results are summarized in Section 6.

2. Observations and Reductions

2.1. Discovery

SN 2022jox was discovered on UT 2022 May 09.26 (MJD 59708.26) by the Distance Less Than 40 Mpc Survey (DLT40; for survey details, see Tartaglia et al. 2018) with an unfiltered brightness of 16.7 mag. The SN is located in the relatively nearby ($D \approx 37.7 \text{ Mpc}$; Tully et al. 2016) galaxy ESO435-G014 (Figure 1) at R.A.(2000) = $09^{\text{h}}57^{\text{m}}44^{\text{s}}480$ and decl. (2000) = $-28^{\circ}30'56''46$ (Bostroem et al. 2022). It was classified less than 2 hr later as a young Type II SN showing flash ionized lines of H I and He (Valenti et al. 2022). A search of Asteroid Terrestrial impact Last Alert System (ATLAS) data (Tonry et al. 2018; Smith et al. 2020) showed a 5σ nondetection limit of $o > 20.35$ on 2022 May 07.03 (MJD 59706.03), or 2.23 days before discovery. This puts fairly tight constraints on the explosion epoch, which is further constrained in the analysis below.

2.2. Imaging

Continuous photometric monitoring was done by the DLT40 survey's two southern telescopes, the PROMPT5 0.4 m telescope at Cerro Tololo International Observatory and the PROMPT-MO 0.4 m telescope at Meckering Observatory in Australia, operated by the Skynet telescope network (Reichart et al. 2005). We observe with the PROMPT5 telescope using no filter (“Open”) and the PROMPT-MO telescope's broadband “Clear” filter, both of which were calibrated to the Sloan Digital Sky Survey (SDSS) *r* band (see Tartaglia et al. 2018 for further reduction details). Aperture photometry on the DLT40 multiband images was performed using Photutils (Bradley et al. 2022) and was then calibrated to the AAVSO Photometric All-Sky Survey (Henden et al. 2009). The last nondetection from

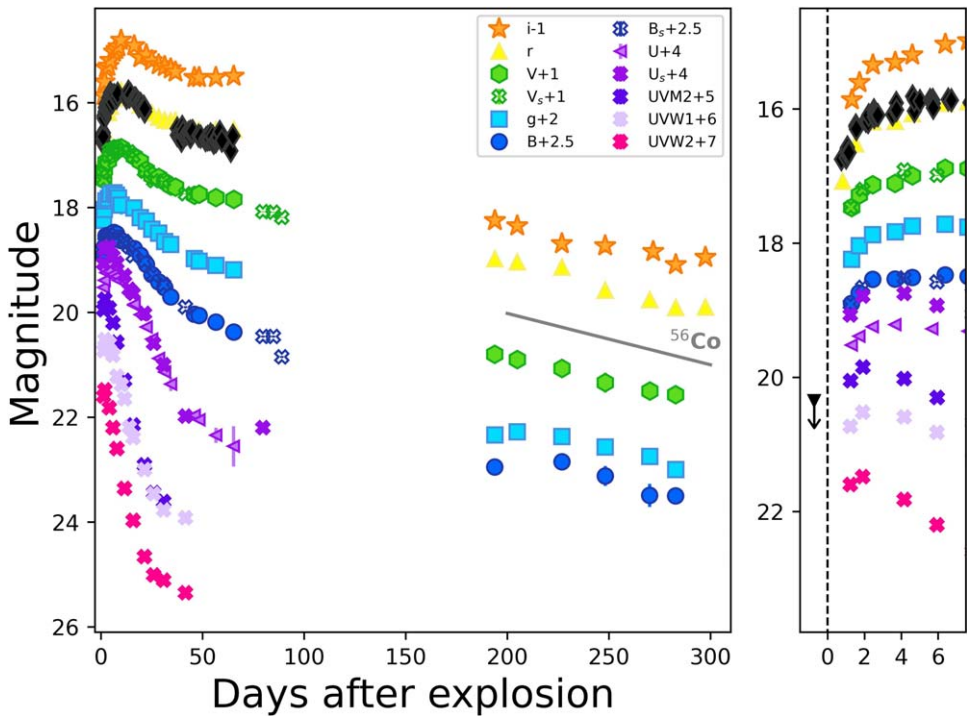


Figure 2. Optical and UV photometry of SN 2022jox, with offsets indicated in the legend. The adopted explosion epoch is MJD 59707.5. Black diamonds are from DLT40, and the X symbols are from Swift. The expected ^{56}Co decay rate is also shown as comparison in gray. The right panel shows a zoom in of the first week, with the 5σ nondetection limit from ATLAS also shown. The data set can be retrieved as the data behind the figure.

(The data used to create this figure are available.)

DLT40 was 2.6 days before discovery, on 2022 May 06.26 (MJD 59705.68), or 1.8 days before the estimated explosion, to a 3σ limiting magnitude of 19.2.

A high-cadence photometric campaign by the Las Cumbres Observatory telescope network (Brown et al. 2013) was begun immediately after discovery in the $UBVgri$ bands with the Sinistro cameras on the 1 m telescopes, through the Global Supernova Project. Using `lcogtsnpipe` (Valenti et al. 2016), a PyRAF-based photometric reduction pipeline, point-spread function fitting was performed. UVB -band data were calibrated to Vega magnitudes (Stetson 2000) using standard fields observed on the same night by the same telescope. Finally, gri -band data were calibrated to AB magnitudes using the SDSS (SDSS Collaboration et al. 2017). The light curves are shown in Figure 2.

Ultraviolet (UV) and optical images were obtained during the early portion of the light curve with the Ultraviolet/Optical Telescope (UVOT; Roming et al. 2005) on board the Neil Gehrels Swift Observatory (hereafter Swift; Gehrels et al. 2004). The data were downloaded from the NASA Swift Data Archive,¹¹ and the images were reduced using standard software distributed with HEAsoft.¹² Photometry was performed for all the $uvw1$, $uvm2$, $uvw2$, U_S -, B_S -, and V_S -band images using a $3''0$ aperture at the location of SN 2022jox. Since no pre-explosion template imaging was available, the contribution from the host galaxy has not been subtracted.

2.3. Spectroscopy

Multiple epochs of spectroscopy were taken spanning 0.8–240 days post explosion. Eight epochs were obtained with the FLOYDS spectrographs (Brown et al. 2013) on the Las Cumbres Observatory’s 2 m Faulkes Telescopes North and South (FTN/FTS) as part of the Global Supernova Project collaboration. One-dimensional spectra were extracted, reduced, and calibrated following standard procedures using the FLOYDS pipeline (Valenti et al. 2014). Five epochs were obtained with the Robert Stobie Spectrograph (RSS) on the Southern African Large Telescope (SALT; Smith et al. 2006). The SALT data were reduced using a custom pipeline based on the PySALT package (Crawford et al. 2010). Four epochs were obtained with the Goodman High Throughput Spectrograph (GHTS-R, GHTS-B; Clemens et al. 2004) on the Southern Astrophysical Research Telescope (SOAR) and reduced using the Goodman pipeline or manually with PyRAF at late phases.¹³ Finally, two epochs were obtained with the Gemini Multi-Object Spectrographs (GMOS; Hook et al. 2004; Gimeno et al. 2016) on the 8.1 m Gemini North and South Telescopes as rapid ToO observations using the B600 grating. Data were reduced using the Data Reduction for Astronomy from Gemini Observatory North and South (DRAGONS) reduction package (Labrie et al. 2019), using the recipe for GMOS long-slit reductions. This includes bias correction, flat-fielding, wavelength calibration, and flux calibration. A log of the spectroscopic observations can be found in Table 1.

¹¹ <https://heasarc.gsfc.nasa.gov/cgi-bin/W3Browse/swift.pl>
¹² <https://heasarc.gsfc.nasa.gov/docs/software/heasoft/>

¹³ Goodman HTS Pipeline Documentation v1.3.6 (2017) <http://soardocs.readthedocs.io/projects/goodman-pipeline/>.

Table 1
Optical Spectroscopy of SN 2022jox

UT Date (yyyy-mm-dd)	MJD	Phase (days)	Telescope+ Instrument	R $\lambda/\Delta\lambda$	Exposure Time (s)
2022-05-09	59708.27	0.8	FTN+FLOYDS	380	1800
2022-05-09	59708.84	1.3	SALT+RSS	1000	1633
2022-05-10	59709.02	1.5	Gemini-S+GMOS	1300	900
2022-05-12	59711.84	4.3	SALT+RSS	1000	1633
2022-05-14	59713.29	5.8	FTN+FLOYDS	380	1800
2022-05-16	59715.24	7.7	Gemini-N+GMOS	1300	900
2022-05-16	59715.53	8.0	FTS+FLOYDS	250	1800
2022-05-18	59717.41	9.9	FTS+FLOYDS	250	1800
2022-05-24	59723.49	16.0	FTS+FLOYDS	250	1800
2022-05-24	59724.06	16.6	SOAR+GHTS-R	850	900
2022-06-01	59731.77	24	SALT+RSS	1000	1633
2022-06-05	59735.77	28	SALT+RSS	1000	1633
2022-06-05	59735.99	29	SOAR+GHTS-R	850	900
2022-06-07	59737.77	30	SALT+RSS	1000	1633
2022-06-13	59743.44	36	FTS+FLOYDS	250	2700
2022-06-23	59753.41	46	FTS+FLOYDS	250	2700
2022-11-17	59900.68	193	FTS+FLOYDS	250	3600
2022-11-29	59912.28	205	SOAR+GHTS-B	850	3600
2023-01-03	59947.29	240	SOAR+GHTS-R	850	3600

Note. Phases are reported with respect to an explosion epoch of MJD 58707.5.

3. Light-curve Analysis

3.1. Distance and Reddening

The heliocentric redshift of the host of SN 2022jox, ESO435-G014, is $z = 0.00889$ (Kregel et al. 2004). Using the most recent Tully–Fisher distance modulus value of $\mu = 32.88 \pm 0.45$ mag (Tully et al. 2016) gives us a distance of $37.7^{+8.6}_{-7.1}$ Mpc, a value we will adopt throughout this paper.

The Milky Way line-of-sight reddening for ESO435-G014 is $E(B - V)_{\text{MW}} = 0.08$ mag (Schlafly & Finkbeiner 2011). We use the prescription of Poznanski et al. (2012) to estimate the host reddening contribution to SN 2022jox by measuring the equivalent width of the Na I D absorption lines from the GMOS-N B600 observation taken on 2022 May 16, resulting in an $E(B - V)_{\text{host}} = 0.013 \pm 0.003$ mag (applying the scaling factor of 0.86). This leads us to $E(B - V)_{\text{tot}} = 0.093$ mag. Comparison with other similar SNe, both in $B - V$ color (Figure 3) and spectroscopy corroborate this fairly low reddening value, which we will use throughout this paper.

3.2. Light-curve Evolution

In Figure 2, we show the full optical and UV light-curve evolution of SN 2022jox over the first ~ 300 days. The V -band light-curve peaks at $M_V = -17.25$ mag, roughly 10 days after explosion (as seen in the bottom panel of Figure 3). This is around the same timescale for the the r and i bands to also reach maximum, which is fairly typical for normal Type II SNe (Anderson et al. 2014a; González-Gaitán et al. 2015; Rubin et al. 2016; Valenti et al. 2016). When compared to other Type II SNe shown in Figure 3, the overall brightness of SN 2022jox is also fainter than objects both with (SN 2017ahn, SN 2014G) and without (SN 2017gmr, SN 2021yja) observed early narrow flash features. This is consistent with the results from Bruch et al. (2023), who found a wide absolute magnitude range for SNe, both with and without flash signatures. What is also interesting is that we observe the rise and peak of the Swift $uvw1$, $uvw2$, and $uvm2$ light curves at roughly 2 days post

explosion. The UV peak is often missed due to the quick cooling of the shock breakout and the lack of extremely early-time observations (Pritchard et al. 2014).

Unfortunately the SN became Sun constrained around 65 days after explosion, and was not visible from the ground for another 130 days when observations were able to begin again. As can be seen in Figure 3 in comparisons with the light curves of other SNe with varying degrees of early flash features, we note that SN 2022jox does not show the classic plateau shapes of Type IIP SNe such as SN 2017gmr, nor does it fall quickly like the Type IIL SN 2017ahn, but instead belongs to a class somewhere in between, most similar to SN 2013ab (Bose et al. 2015). Interestingly, one of the earliest descriptions of Type II SNe from Barbon et al. (1979) describes an initial steeper decline followed by a plateau period before another decline to what we now know indicates the transition to the radioactive tail phase, similar to the behavior exhibited here. In particular, using the definitions of s_1 and s_2 from Anderson et al. (2014b), there is a pronounced initial steeper slope of $s_1 = 2.65$ mag 100 day^{-1} followed by a much shallower second slope $s_2 = 0.8$ mag 100 day^{-1} . We caution that the value for s_2 may not be precise, as data are limited around the end of the plateau.

While there may not be comprehensive coverage of the light curves leading up to and during the fall from the plateau, when photometry began again on day 195, the light curve had dropped by 2.7 mags in the V band. From here the light curves evolve at values consistent with a radioactive decay of 0.0098 mag day^{-1} (e.g., Woosley et al. 1989), as shown in Figure 2.

3.3. Color Evolution

The color evolution of SN 2022jox behaves similarly to other well-studied Type II SNe. As we show in the top panel of Figure 3, the $B - V$ color starts out fairly blue at $B - V = -0.2$ mag, but then redden as the ejecta expand and cool reaching a $B - V$ color of ~ 0.9 mag before the SN becomes Sun constrained. Once the SN is observable again it is

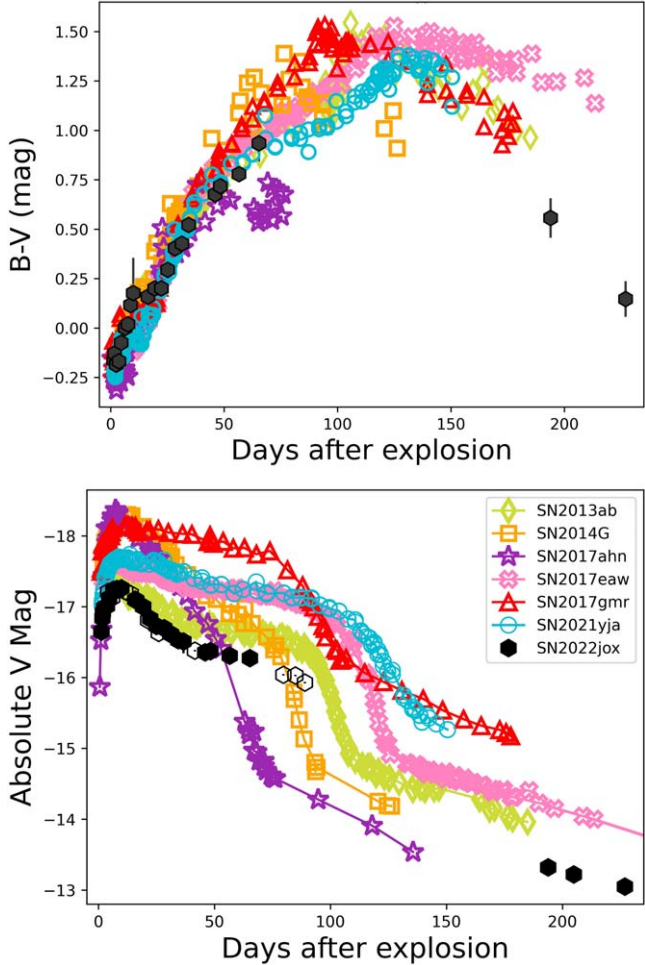


Figure 3. Top: $B - V$ color evolution of SN 2022jox compared with other Type II SNe. Bottom: Absolute V-band photometry of the same objects above. The open symbols for SN 2022jox indicate Swift V_S photometry. Data are from Bose et al. (2015, SN 2013ab), Terreran et al. (2016, SN 2014G), Tartaglia et al. (2021, SN 2017ahn), Szalai et al. (2019, SN 2017eaw), Andrews et al. (2019, SN 2017gmr), and Hosseinzadeh et al. (2022, SN 2021yja), and have all been corrected for reddening and distances from values within. Legend is the same for both figures.

in the radioactive decay phase, and quite blue compared to other SNe at similar times. While B -band data at late times of CCSNe can be sparse, comparison with the normal Type II SN 2017eaw shows SN 2022jox to be bluer by roughly 0.75–1.0 mag around day 200.

There are two possibilities for the very blue color of SN 2022jox, both of which indicate the late-time $B - V$ color needs to be viewed with caution. One explanation is that the B -band photometry is actually contaminated by a host star cluster, which if young could be quite blue. The alternative is that increased CSM interaction is producing extra blue flux. This is often seen in Type IIn SNe with strong interaction where a forest of Fe emission lines emerge and creates a blue pseudo-continuum (Smith et al. 2009; Moran et al. 2023). For other Type II SNe, though, weaker CSM interaction can manifest as an overall shift to bluer emission (Dessart et al. 2023), although this generally happens much later in the evolution. Note that the spectra of SN 2022jox taken around day 200 do not show any obvious extra blue flux, but the spectra were taken for red optimization so we cannot rule this possibility out.

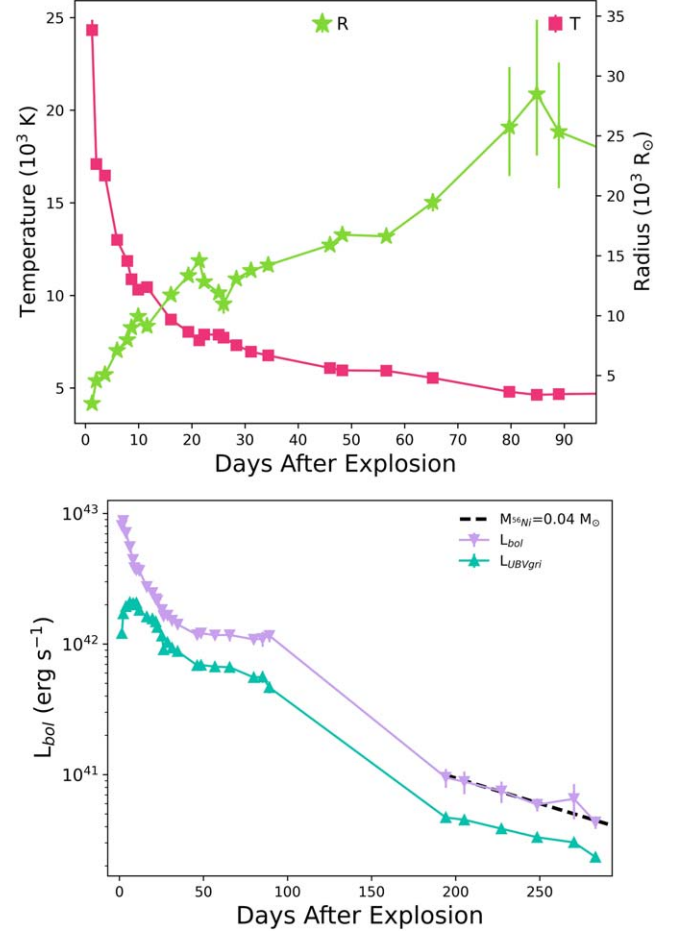


Figure 4. Blackbody temperature, radius (top), and luminosity (bottom) evolution of SN 2022jox derived from the UV to optical photometry. All data have been dereddened by our assumed $E(B - V)_{\text{tot}} = 0.093$ mag. Temperature and radius are derived from fitting the Planck function to the photometry using an MCMC routine. Both the derived bolometric (purple) and pseudo-bolometric (cyan) luminosity are shown.

3.4. Bolometric Light Curve and ^{56}Ni Mass

In the bottom panel of Figure 4, we show the bolometric and pseudo-bolometric light curves of SN 2022jox constructed from the Light Curve Fitting Package (Hosseinzadeh et al. 2023a). For the bolometric luminosity, at each epoch a blackbody spectrum was fit to the observed spectral energy distribution using a Markov Chain Monte Carlo fitting routine. This results in a maximum $L_{bol} = 8.0 \times 10^{42}$ erg s $^{-1}$. For the pseudo-bolometric light curve the best-fit blackbody is integrated only from U to i and peaks at $L_{bol} = 2.1 \times 10^{42}$ erg s $^{-1}$. For the first ~ 50 days the light curve was constructed including the Swift data, but the epochs during the radioactive tail phase are derived only from $BVgri$ photometry (as seen in Figure 2).

The late-time luminosity decline is similar to that of the fully trapped ^{56}Co decay of $0.0098 \text{ mag day}^{-1}$ (dashed line in Figure 4). We explore this more below, but this indicates that no substantial additional luminosity is being produced by ongoing CSM interaction. To estimate the ^{56}Ni mass, we turn to the methods described in Hamuy (2003), Jerkstrand et al. (2012), and Pejcha & Prieto (2015), all of which employ the radioactive tail of the bolometric light curve. This results in measured ^{56}Ni masses of $0.041 \pm 0.001 M_\odot$, $0.039 M_\odot \pm 0.001$, and $0.046 \pm 0.003 M_\odot$, respectively, and an average ^{56}Ni mass

Table 2
Shock-cooling Parameters Plotted in Figure 5

Parameter	Variable	Prior			Best-fit Values ^a		Units
		Shape	Min.	Max.	MSW23	SW17	
Shock velocity	v_{s*}	Uniform	0	5	4.1 ± 1.0	$3.2_{-0.3}^{+0.6}$	10^3 km s^{-1}
Envelope mass	M_{env}	Uniform	0	5	$1.0_{-0.3}^{+0.5}$	$1.2_{-0.2}^{+0.4}$	M_{\odot}
Ejecta mass \times numerical factor	$f_{\rho} M$	Uniform	1	100	4_{-3}^{+9}	20_{-20}^{+40}	M_{\odot}
Progenitor radius	R	Uniform	0	1436	633_{-129}^{+201}	718 ± 144	R_{\odot}
Explosion time	t_0	Uniform	-1.0	1.0	0.5 ± 0.1	0.2 ± 0.1	MJD - 59707
Intrinsic scatter	σ	Log-uniform	0	100	$4.9_{-0.3}^{+0.4}$	4.5 ± 0.3	...

Note.

^a The “Best-fit Values” columns are determined from the 16th, 50th, and 84th percentiles of the posterior distribution, i.e., median $\pm 1\sigma$. MSW23 and SW17 stand for the two models from Morag et al. (2023) and Sapir & Waxman (2017), respectively. The former is preferred.

of $0.044 \pm 0.003 M_{\odot}$. Because the Pejcha & Prieto (2015) calculation is based on the bolometric luminosity for day 200, we interpolate the light curve for this epoch and obtain an $L_{\text{bol}} = 9.26 \times 10^{40} \text{ erg s}^{-1}$. Average values for ^{56}Ni masses in normal Type II SNe have been found to be $\sim 0.04 M_{\odot}$ (Valenti et al. 2016; Müller et al. 2017; Anderson 2019; Rodríguez et al. 2021), indicating SN 2022jox is a perfectly average object in this regard. We note that these values are highly dependent on the distance used.

The resultant temperature and radius evolution derived from the bolometric luminosity are also shown in the top panel of Figure 4. The behavior of both quantities is similar to that of other Type II SNe, where the temperature falls from maximum to a steady value over the same time period when the radius increases to maximum. In SN 2022jox, T_{BB} drops from $\sim 25 \text{ kK}$ within a day of explosion, to settle into values near 5 kK after about 2 months. During this same time period R_{BB} increases to a maximum value of $2.8 \times 10^4 R_{\odot}$ as it approaches the nebular phase.

3.5. Shock-cooling Modeling

In order to constrain the radius of the progenitor and the date of explosion, we follow the methods presented in Hosseinzadeh et al. (2023b), and compare the model fits from both Morag et al. (2023, hereafter MSW23) and Sapir & Waxman (2017, hereafter SW17). The MSW23 models are built upon the previous SW17 models, with the main difference being that it considers the line blanketing in the UV at early times instead of assuming a blackbody at all epochs. Moreover, SW17 is valid at the earliest phases when the stellar radius is larger than the thickness of the emitting shell. As we describe below, this causes some differences in the best-fitting parameters to the data.

Using 25 walkers, both models reached convergence with 3000 steps, with an additional 3000 steps for posterior sampling. The model was valid over the date range used of MJD 59706.0–59715.2. A full comparison, along with the description of each input parameter, is shown in Table 2 and a graphical representation of each model fit is shown in Figure 5. For these models, the progenitor is assumed to be a polytrope with a density profile $\rho_0 = \frac{3f_{\rho}M}{4\pi R^2}\delta^n$, where f_{ρ} is a numerical factor of order unity, M is the ejecta mass (minus the remaining remnant), R is the progenitor radius, $\delta \equiv \frac{R-r}{R}$ is the fractional depth from the stellar surface, and $n = \frac{3}{2}$ is the polytropic index for convective envelopes. Additionally, the shock

velocity profile, $v_{\text{sh}} = v_{s*}\delta^{-\beta n}$, where v_{s*} is a free parameter and $\beta = 0.191$ is a constant, the explosion time is t_0 , M_{env} is the mass in the stellar envelope, and σ is an intrinsic scatter term.

There are a few discrepancies between the two models, one being the significant underprediction of the UV flux in the MSW23 model a few days after peak, and another being the larger best-fit values for $f_{\rho}M$ in the SW17 models. The differences in UV fitting is likely due to the inclusion of line blanketing in MSW23. Other best-fit parameter values between the two models are consistent with each other. Due to the way that $f_{\rho}M$ is weakly constrained in SW17, we will defer to the MSW23 results for the physical interpretation of the explosion of SN 2022jox, as was done for SN 2023ixf and SN 2023axu (Hosseinzadeh et al. 2023b; Shrestha et al. 2024).

We find a best-fit progenitor radius from MSW23 of $R = 633_{-129}^{+201} R_{\odot}$, which is squarely in accepted ranges of RSG radii. The best-fit explosion epoch is MJD 59707.5 ± 0.1 . For reference, the DLT40 discovery occurred on MJD 59708.26, 0.76 days after the estimated explosion, and the ATLAS nondetection was 1.4 days before estimated explosion, in good agreement with this explosion epoch. These numbers are presented with some caution though, because, as we discuss below, there is evidence for early CSM interaction from spectral observations, which can change the luminosity evolution (Morozova et al. 2017, 2018). This could partially explain the underestimation for the UV flux we see in Figure 5 from the models, particularly in MSW23. Another potential factor could be an overestimation of the line blanketing in the MSW23 model (although that is not a factor for the SW17 models, which still underpredict the UV flux as well).

4. Spectroscopic Evolution

Optical spectra of SN 2022jox were obtained from 0.8 day to 240 days post explosion, with high cadence over the first month. As we show in Figure 6, our earliest spectra with FLOYDS, SALT, and Gemini-S reveal narrow emission lines, which are gone by our next observation on day 4.3. The spectra then become mostly featureless from 6 to 10 days post explosion, only to then become dominated by broad (7000 km s^{-1}) Balmer emission, as shown in Figure 7. There is a gap of spectral coverage between days 46 and 194, but the late-time spectra shown in the bottom panel of Figure 7 show somewhat normal nebular spectral features, including intermediate-width H α , oxygen, and calcium emission lines. Note that there is some contamination from the surrounding H II

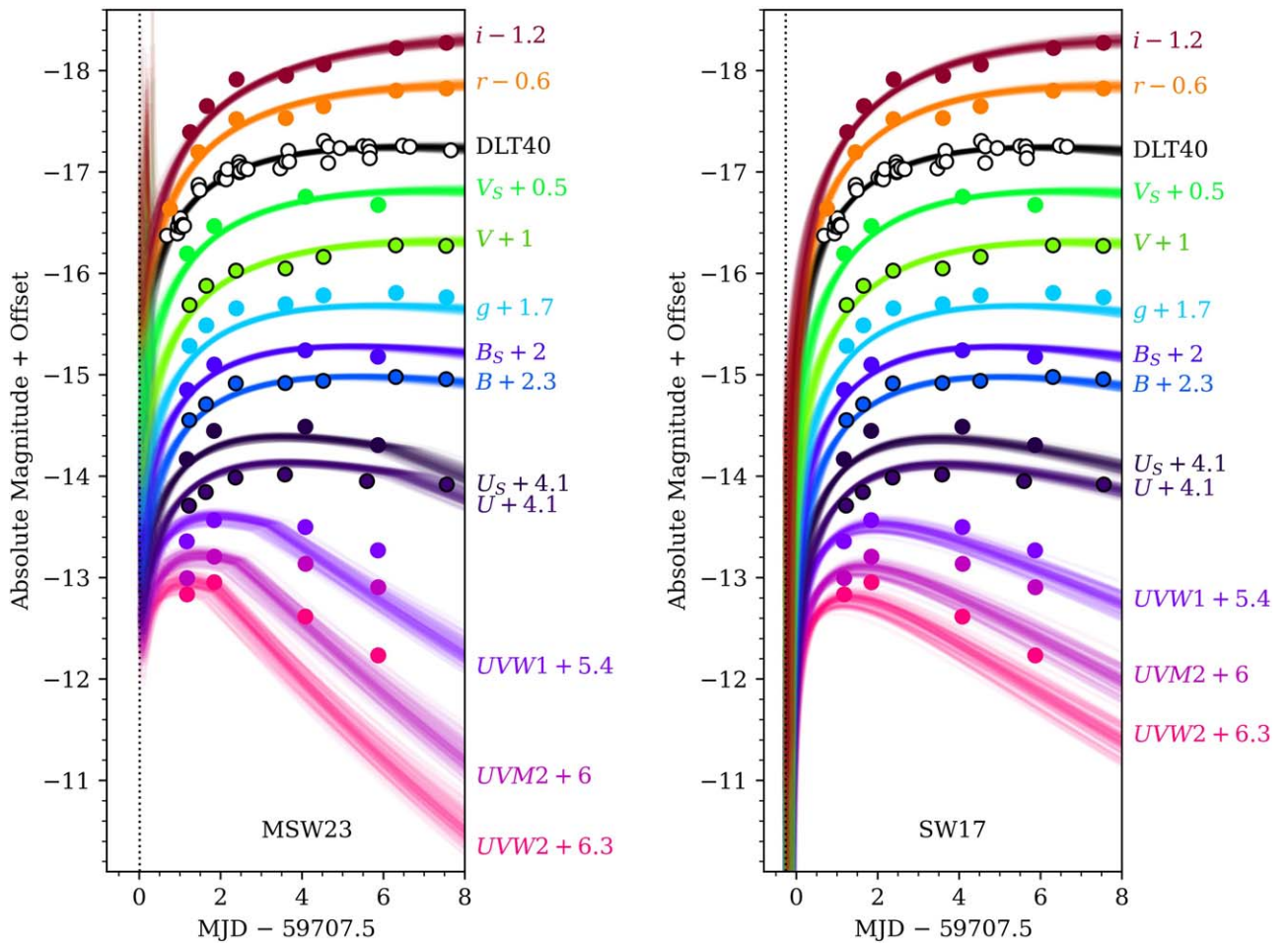


Figure 5. Shock-cooling fit to SN 2022jox data using Morag et al. (2023, left) and Sapir & Waxman (2017, right). The explosion epoch is indicated by a dotted line. The best-fit values are shown in Table 2.

region in all epochs (marked by dotted lines), but most features can be attributed to the SN itself, as we discuss in detail below.

4.1. Early Spectroscopy and Comparison with Other Supernovae with Flash Features

In the first few epochs of optical spectra taken at 0.8, 1.3, and 1.5 days after explosion, we see narrow Balmer lines (in particular, $H\alpha$ and $H\beta$), He II $\lambda 4686$ and $\lambda 5412$, C IV $\lambda\lambda 5801$, 5811, and N IV $\lambda\lambda 7109$, 7123 (Figure 6). As we show in Figure 8, $H\alpha$ at these early times can be reproduced with a combination of a narrow Gaussian (FWHM = 300 km s $^{-1}$) on top of a broader Lorentzian (FWHM = 1700 km s $^{-1}$). Due to the width of the Gaussian being similar to the instrumental resolution at these epochs, it is hard to tell how much of the narrow contribution is from the SN and from the H II region, but the presence of other lines such as [O III] and [S II] show that there is some contamination.

By our next spectrum on day 4.3, only the Balmer lines show narrow emission (likely with some contribution from the host galaxy). Now, in place of the narrow He II $\lambda 4686$ emission, a broad feature, sometimes referred to as a “ledge,” appears blueshifted from He II (Andrews et al. 2019; Soumagnac et al. 2020; Hosseinzadeh et al. 2022). A day and a half later, 5.8 days after explosion, the feature is completely gone. Considering that the location and width of the ledge in SN 2022jox lines up well with the blue edge of 1.3 days He II

$\lambda 4686$ emission, we can postulate that it is a blend of N III/C III which only becomes detectable as the strength of He II fades. Early spectra of other SNe II have also shown a broad feature around 4600 Å, as shown in Figure 9, and discussed in detail in the recent papers on SN 2018lab (Pearson et al. 2023) and SN 2023axu (Shrestha et al. 2024). While in some instances a blend of N III/C III is most likely, it is also possible that in a few cases it could be from a broad and blueshifted He II line, specifically when the feature is extremely broad as in SN 2017gmr (Andrews et al. 2019) or SN 2013fs (Bullivant et al. 2018).

While the optical spectra become fairly featureless by the end of the first week, $H\alpha$ is still present, minus the Lorentzian wings. By 7.7 days, a narrow P-Cygni profile is seen, with the same narrow Gaussian emission (FWHM = 300 km s $^{-1}$) present as in the day 1.3 spectrum but now with an additional Gaussian absorption feature (FWHM = 580 km s $^{-1}$), as shown in the bottom panel of Figure 8. We will discuss the implications of this absorption feature in Section 4.3. Finally, by day 9.9, a broad, blueshifted $H\alpha$ emission profile emerges from the featureless blue continuum, behavior typical for Type II SNe.

The early spectroscopy of SN 2022jox can be compared with other Type II SNe showing flash signatures, in particular the recent SN 2023ixf, and the well-studied SN 2014G, SN 2013fs, SN 2017ahn, and SN 2020pni. In terms of similar spectral evolution, we find that the best match is to SN 2014G, and to

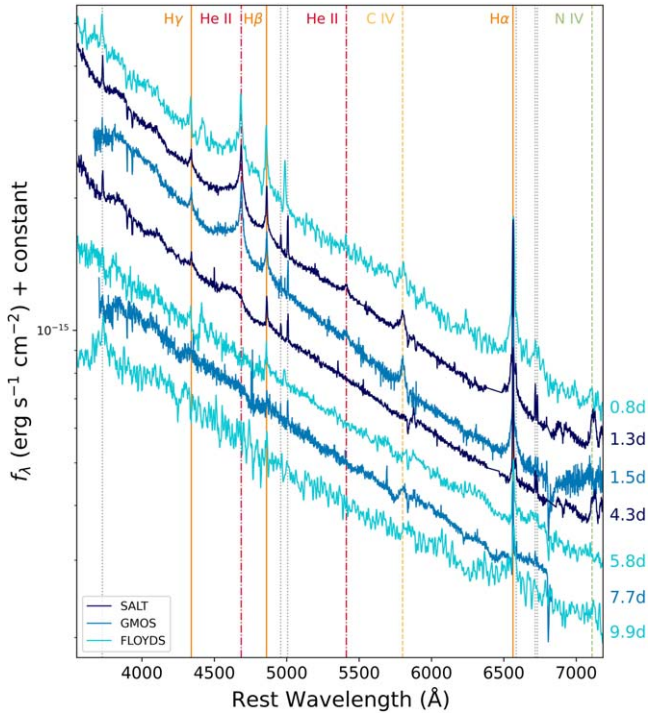


Figure 6. Optical spectra of SN 2022jox for the first 10 days after explosion. Each telescope+instrument pair is noted by a different color. Notable lines are identified, and H II region lines are marked with dotted gray lines. The dates are with respect to our assumed explosion epoch of MJD 59707.5.

(The data used to create this figure are available.)

an extent SN 2023ixf (but shifted temporally by ~ 1.5 days). It may be the case that this temporal shift is not real, but that the estimated explosion epochs on more distant objects can be off by as much as a day or so because they are just too faint to observe during this early phase. In comparison with SN 2023ixf, SN 2022jox is at a distance 5 times further away.

A comparison between SN 2022jox, SN 2014G, and SN 2023ixf is shown in Figure 10. Unfortunately, we do not have any spectra between 1.5 and 4.3 days for SN 2022jox, and no spectra earlier than 2.5 days for SN 2014G, but the day 1.5 spectrum of SN 2022jox is almost identical to that of SN 2014G at 2.5 (and 3.5) days. This includes the lack of narrow N III/C III, and the presence of weak He II and prominent C IV. The width and the continuum-normalized flux of H α are almost identical as well. As the flash features fade, the 7.7 days (SN 2022jox) and 9.3 days (SN 2014G) spectra are almost identical in the featureless spectra.

We also get decent matches if we compare later epochs of SN 2023ixf to earlier epochs of SN 2022jox. For instance, while the 1.5 days SN 2023ixf spectrum (shown at the top of Figure 10) shows narrow N III/C III, and rather strong He II and broader H α , if we compare the 3.2 days SN 2023ixf spectrum to the 1.5 days spectrum of SN 2022jox we get an almost identical match. Similarly, the 4.3 days SN 2022jox spectrum is traced fairly well by the 7.6 days SN 2023ixf spectrum, including the broad feature where the N III/C III and He II narrow lines once were. This could suggest a difference between the CSM or the energetics of the two SNe, which we will discuss more below in Section 5, or, as we mention above, could just be due to incorrect explosion epochs (i.e., SN 2022jox is actually older than we estimate).

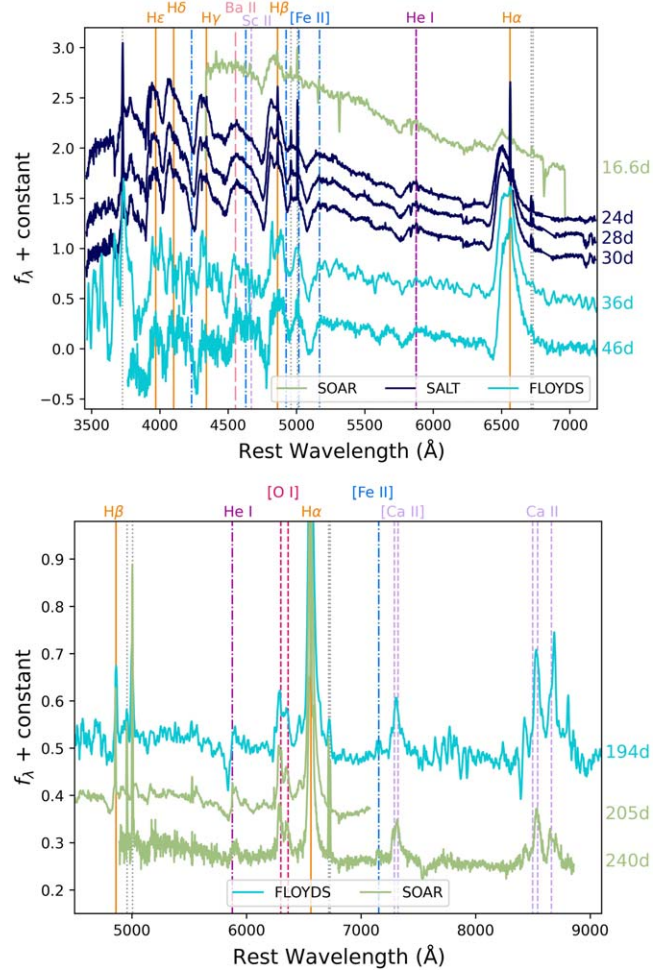


Figure 7. Same as for Figure 6 but 16.6–46 days (top) and 194–240 days (bottom) post explosion.

(The data used to create this figure are available.)

4.2. Later Times

Starting with our 16.6 days spectrum (Figure 7, top panel), we begin to see broad hydrogen emission lines from the fast-moving ejecta as the photosphere begins to cool. During the next month many Fe lines appear in the blue end of the spectrum, including Fe II $\lambda\lambda$ 4924, 5018, and λ 5169 as well as He I in emission. Our first few weeks of spectra were taken with instruments configured for the bluest wavelengths, so the early evolution of [Ca II] and the Ca II infrared (IR) triplet were missed.

The last three epochs of spectroscopy were taken over 150 days later, well into the radioactive tail of the evolution (Figure 7, bottom panel). These spectra reveal much narrower H α emission along with [O I] $\lambda\lambda$ 6300, 6363, [Ca II] $\lambda\lambda$ 7291, 7324, and the IR triplet of Ca II $\lambda\lambda$ 8498, λ 8542, λ 8662, as well as very weak Fe II λ 7155. H II region lines are particularly strong in the late-time spectra due to the fading of the SN and its location in a complex environment.

One notable feature in the nebular spectra is an emission line at ~ 6460 Å (or at ~ -4670 km s $^{-1}$ from the center of H α) seen in our 194 and 205 days spectra (Figure 11), which is mostly gone in our final spectrum at 240 days. A very similar feature was seen in SN 2014G and reported in Terreran et al. (2016, their

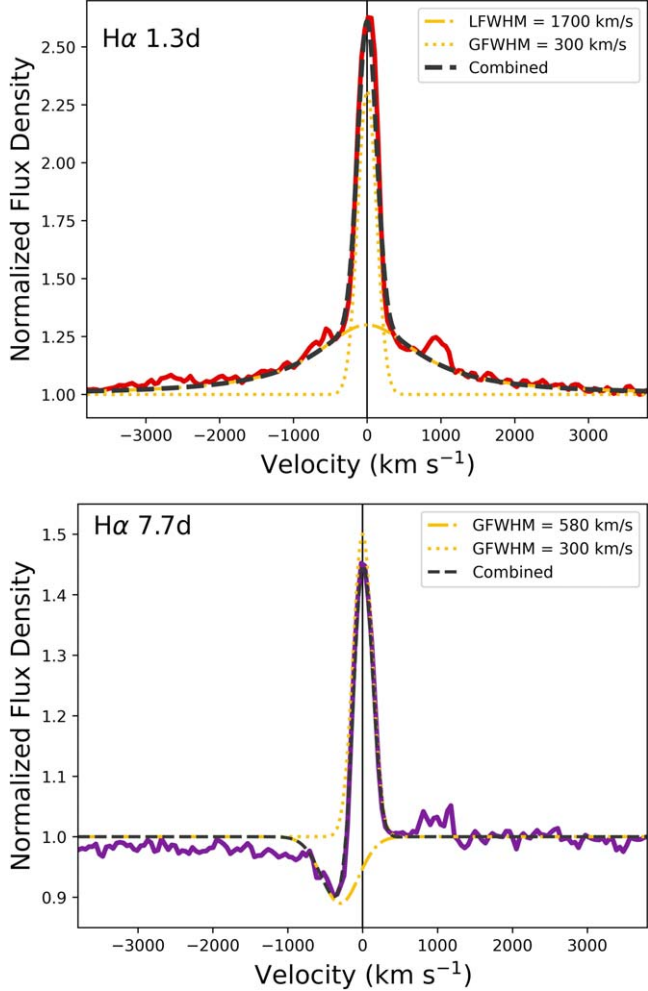


Figure 8. Multicomponent Gaussian and Lorentzian fits to the narrow and intermediate $H\alpha$ components at 1.3 days (top) and 7.7 days (bottom) after explosion. Both can be fit with a Gaussian centered at 0 km s^{-1} with a $\text{FWHM} = 300\text{ km s}^{-1}$ plus intermediate-width Lorentzian emission on day 1.3 or a narrow Gaussian absorption by day 7.7. Both spectra have been normalized to the local continuum.

Figure 10) with a centroid closer to 6400 \AA , and noticeable redward evolution over ~ 100 days from -7580 to -6755 km s^{-1} . The authors ultimately attributed this to the start of the outer ejecta interacting with highly bipolar CSM, with the red side being obscured by radiative-transfer and/or geometry effects. This conclusion was partly due to fitting a day 387 spectrum of SN 2014G with two symmetric but boxy profiles on either side of $H\alpha$ to reproduce a bridge between $H\alpha$ and $[\text{O I}]$. We may be seeing a similar bridge starting to form in our last spectrum of SN 2022jox on day 240, but later-time observations are needed for confirmation. Also of note is that the expansion velocity of SN 2022jox from the $H\alpha$ width on day 194 is roughly half that of SN 2014G at nearly the same epoch. This may also have some bearing on the location of the blue bump feature.

A somewhat similar, but more symmetrical feature was seen in the nebular spectra of SN 1998S and was attributed to interaction with a disk of CSM (Fransson et al. 2005). As we show in Figure 11, the wavelength of the blue feature in SN 1998S lines up fairly well with the one in SN 2022jox. Additionally, in SN 1998S there is a distinct red feature and a much less pronounced central peak, which could be due to the

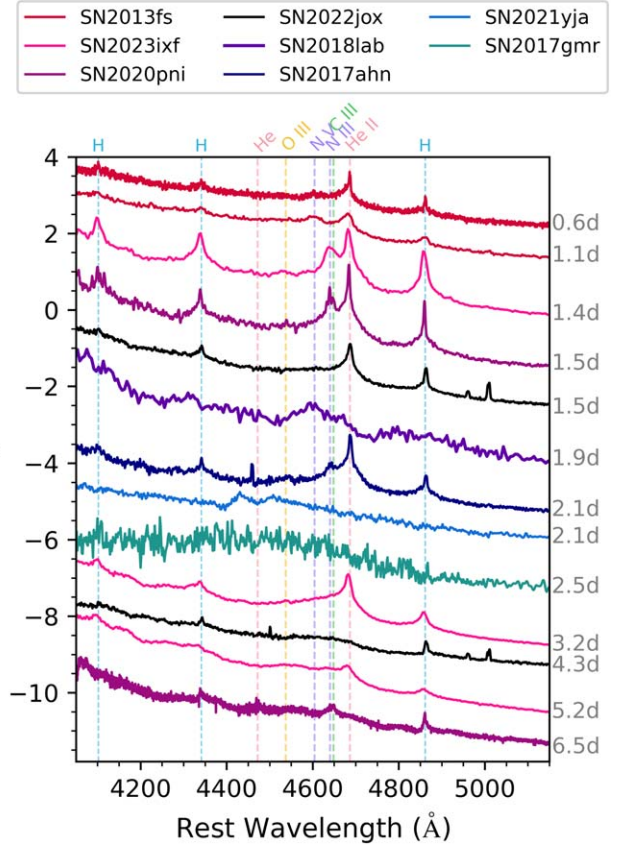


Figure 9. The 1.5 days and 4.3 days optical spectrum of SN 2022jox centered around 4600 \AA compared to early-time spectra of SN 2013fs (Bullivant et al. 2018), SN 2013ixf (Bostroem et al. 2023), SN 2020pni (Terreran et al. 2022), SN 2018lab (Pearson et al. 2023), SN 2017ahn (Tartaglia et al. 2021), SN 2021yja (Hosseinzadeh et al. 2022), and SN 2017gmr (Andrews et al. 2019). SN 2022jox clearly evolves from narrow emission similar to SN 2013fs and SN 2017ahn (minus the N III/C III emission) to a broader blended feature more similar to SN 2018lab and SN 2017gmr. All spectra have been corrected for extinction.

differences in epochs. The presence of this additional $H\alpha$ feature in SN 2022jox could suggest that there was an outer asymmetric CSM surrounding the progenitor separate from the inner CSM creating the flash features seen in the first few days. The Type II SN 2007od also showed a similar peak at -5000 km s^{-1} , starting at day 232 and persisting for at least another year and a half, which was attributed to late-time CSM interaction (Andrews et al. 2010). Without additional nebular spectra of SN 2022jox at this point we cannot explore this further, although more data are expected in the coming observing semesters and will shed more light on the evolution of the progenitor of SN 2022jox.

4.3. $H\alpha$ Evolution

The evolution of $H\alpha$ in velocity space is shown in Figure 12. As mentioned above, the three earliest spectra of SN 2022jox show a strong narrow $H\alpha$ core along with broad Lorentzian wings, caused by multiple electron scatterings in an optically thick material. In the SALT spectrum from day 1.3 (Figure 8, top panel), the line can be well fit by a combination of a Gaussian profile with an $\text{FWHM} = 300\text{ km s}^{-1}$ and a Lorentzian with an $\text{FWHM} = 1700\text{ km s}^{-1}$, and wings that extend to roughly $\pm 3000\text{ km s}^{-1}$, both centered at zero velocity. The resolution of SALT RSS spectra around $H\alpha$ is

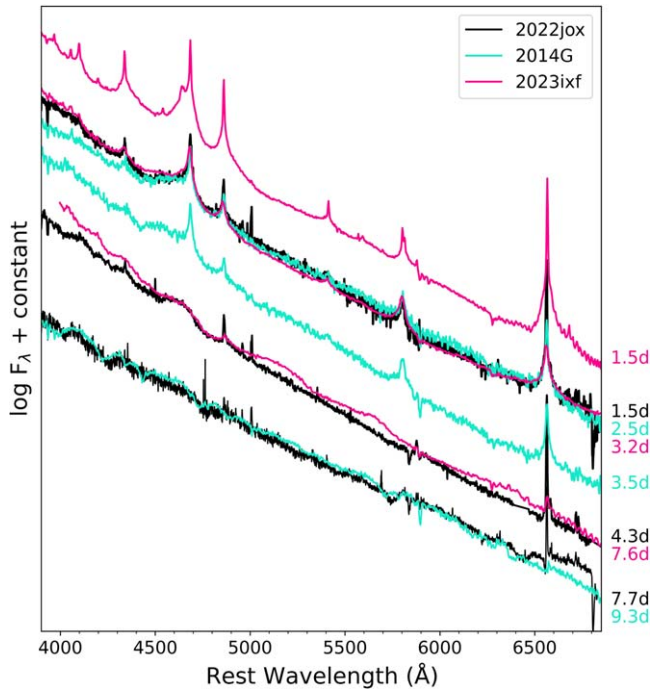


Figure 10. Comparison of early spectra of SN 2022jox to similar features seen in SN 2014G and SN 2023ixf. Note that the 1.5 days SN 2022jox spectrum matches the 3.2 days SN 2023ixf spectrum, indicating a ~ 1.5 days lag in evolution between the two objects. Data are from Terreran et al. (2016) and Bostroem et al. (2023).

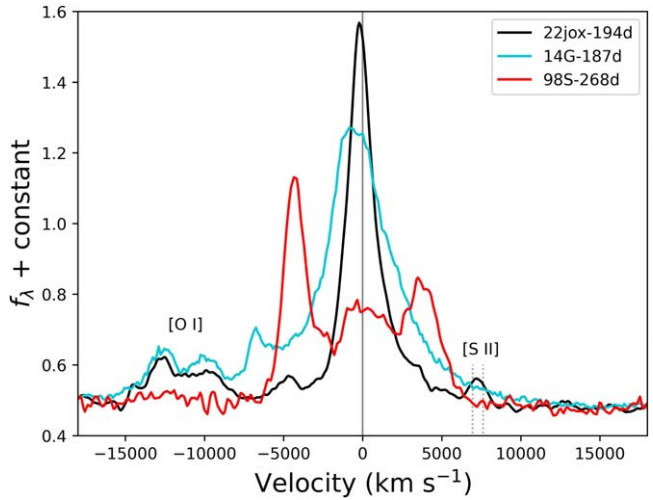


Figure 11. Comparison of our day 194 spectrum of SN 2022jox with the 187 days spectrum of SN 2014G (Terreran et al. 2016) and the 268 days spectrum of SN 1998S (Fransson et al. 2005), centered around $\text{H}\alpha$. The prominent blueshifted feature can be seen between $\text{H}\alpha$ and $[\text{O I}]$. Only SN 1998S has a corresponding symmetrical redshifted feature.

$\sim 315 \text{ km s}^{-1}$, so it is likely the narrow line is not resolved, and also may have some contamination from the H II region. By 4.3 days the the Lorentzian wings of $\text{H}\alpha$ have decreased to $\pm 1300 \text{ km s}^{-1}$.

On day 7.7, the Lorentzian profile has completely disappeared, leaving behind a narrow P-Cygni profile (Figure 8, top panel). This profile can be recreated with the same narrow emission Gaussian with $\text{FWHM} = 300 \text{ km s}^{-1}$ along with an absorption feature with $\text{FWHM} = 580 \text{ km s}^{-1}$, centered at -300 km s^{-1} , with the blue edge extending to roughly

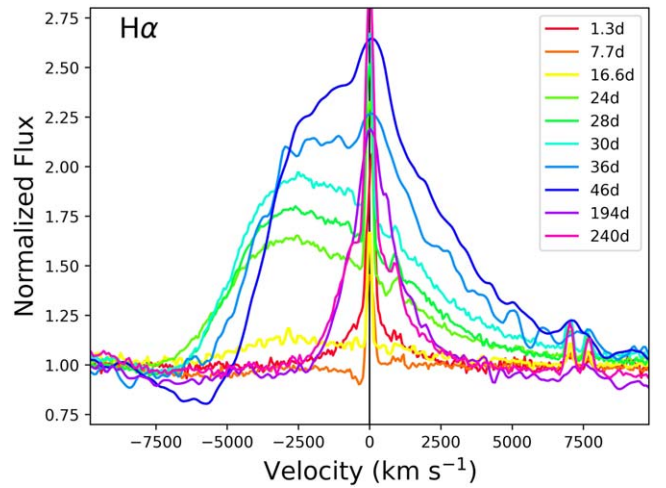


Figure 12. $\text{H}\alpha$ evolution from selected spectra. The lines have been normalized to the local continuum.

-700 km s^{-1} . This absorption feature is likely caused by unshocked CSM along our line of sight and is gone in our next spectrum taken ~ 2 days later, possibly representing a transition to the ejecta being fully outside of the CSM. Indeed, the higher velocities of up to 700 km s^{-1} traced by the wings of the absorption profile could indicate accelerated CSM ahead of the shock, as this value is much higher than expected for steady RSG or LBV winds (although eruptive wind velocities cannot be ruled out).

Over the following few weeks broad, blueshifted $\text{H}\alpha$ appears, centered around -2800 km s^{-1} . This is a common feature of Type II SNe, as a result of the steep density profiles in the SN ejecta and the thick hydrogen envelope obscuring the receding side (Dessart & Hillier 2005; Anderson et al. 2014a). As $\text{H}\alpha$ strengthens, the center shifts inward and the P-Cygni absorption becomes more pronounced, an indication that the optical depth has greatly decreased. Although, at least by our last epoch before the nebular phase on day 46, it is fairly weak as compared to other Type II. Little or no broad absorption is often seen in Type II SN with signs of CSM interaction, particularly in Type IIn. This could indicate that a lower degree of CSM interaction is occurring well into the second month after eruption. As the photospheric phase ends and the recombination has moved through the envelope, the lines become more symmetric. When we begin observations again on day 194, the $\text{H}\alpha$ FWHM has become centralized and has decreased to $\sim 2300 \text{ km s}^{-1}$, and the possible high-velocity feature discussed above has appeared at -5000 km s^{-1} .

We have fit the $\text{H}\alpha$ emission profile from our day 240 spectrum (Figure 13), deconvolving the SN emission from the narrow H II region lines. From a single Lorentzian with an $\text{FWHM} = 2500 \text{ km s}^{-1}$, we measure an $F_{\text{H}\alpha} = 1.3 \times 10^{-14} \text{ erg s}^{-1} \text{cm}^{-2} \text{ Å}^{-1}$. At a distance of 37.7 Mpc, $\text{Log}(L_{\text{H}\alpha}) = 39.62$. For comparison, SN 1998S, which was classified as a Type IIn with known CSM interaction, had a $\text{Log}(L_{\text{H}\alpha}) = 40.09$ on day 300 (Mauerhan & Smith 2012), which suggests less CSM interaction is contributing to the late-time luminosity of SN 2022jox. As discussed and shown in Mauerhan & Smith (2012), the $\text{Log}(L_{\text{H}\alpha})$ of SN 1998S declined at the same rate as ^{56}Co decay over the first 1000 days, then stalled out at a relatively constant luminosity, likely due to the contribution from SN/CSM interaction. As we show above in Figures 2 and 4, our last epochs of photometry suggest a

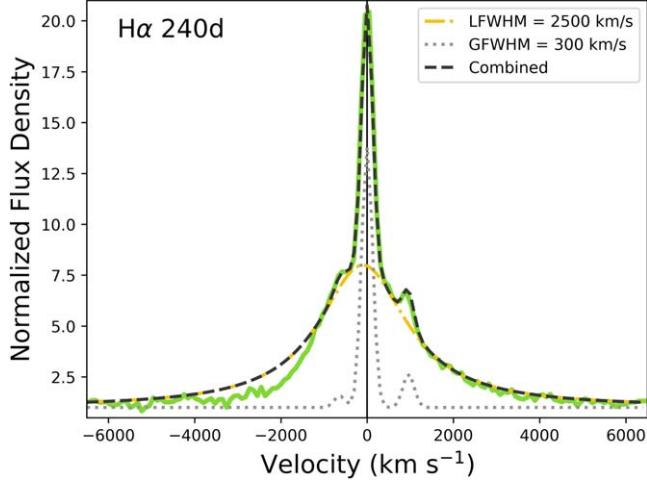


Figure 13. Multicomponent Gaussian and Lorentzian fits to $\text{H}\alpha$ on day 240. The narrow H II region lines of $\text{H}\alpha$ and $[\text{N II}]$ can be fit by Gaussians with $\text{FWHM} = 300 \text{ km s}^{-1}$ and are shown as dotted gray lines. The remaining SN emission can be fit by a slightly blueshifted (-100 km s^{-1}) Lorentzian with a $\text{FWHM} = 2500 \text{ km s}^{-1}$ (shown in yellow). The spectrum has been normalized to the local continuum.

decline consistent with ^{56}Co decay, with no major contribution from CSM interaction. The late-time $\text{H}\alpha$ profiles do show Lorentzian wings, though, which could be a sign of low-level interaction still occurring. If we continue to observe SN 2002jox, we may see a deviation from ^{56}Co decay once the power source from radioactive decay reaches a level below that contributed by the CSM interaction.

Using the blue edge of the $\text{H}\alpha$ absorption that becomes visible on day 9.9 of 8500 km s^{-1} , we can estimate the shock has reached a distance of roughly $7.3 \times 10^{14} \text{ cm}$ by this date, and it would be between 3.2 and $4.3 \times 10^{14} \text{ cm}$ between 4.3 and 5.8 days when the bulk of the narrow features disappear. This puts a limit on the extent of the (dense) CSM. Using the canonical wind velocity of 50 km s^{-1} would indicate a mass-loss event happening 2 – 3 yr prior to explosion. If instead we use a wind velocity of 700 km s^{-1} measured from the edge of the $\text{H}\alpha$ P-Cygni absorption line in the 7.7 days spectrum, this would suggest a mass-loss event only 50 – 70 days prior. There was no pre-explosion eruption detected in archival data, which is not entirely unexpected as at a distance of 37.7 Mpc only events brighter than -13 to -14 mag would be seen by most surveys. This is brighter than expected from pre-supernova eruptions of RSGs, which would range from $-8 < M_r < -10$ mag (Davies et al. 2022; Dong et al. 2023; Tsuna et al. 2023).

5. Analysis

5.1. Model Comparison at Early Times

We have compared our early spectra with non-LTE radiative-transfer models from Dessart et al. (2017). These models assume a $15 M_\odot$ RSG with $R_\star = 501 R_\odot$ with various mass-loss rates, and span the time period from shock breakout to roughly 15 days post explosion. The wind velocity, $v_w = 50 \text{ km s}^{-1}$, extends to $5 \times 10^{14} \text{ cm}$, at which point the mass-loss rate drops to $10^{-6} M_\odot \text{ yr}^{-1}$. A complete summary of the parameters of each publicly available model can be found in Table 1 of Dessart et al. (2017). For SN 2022jox, the best matches are achieved using the rather high mass-loss rate

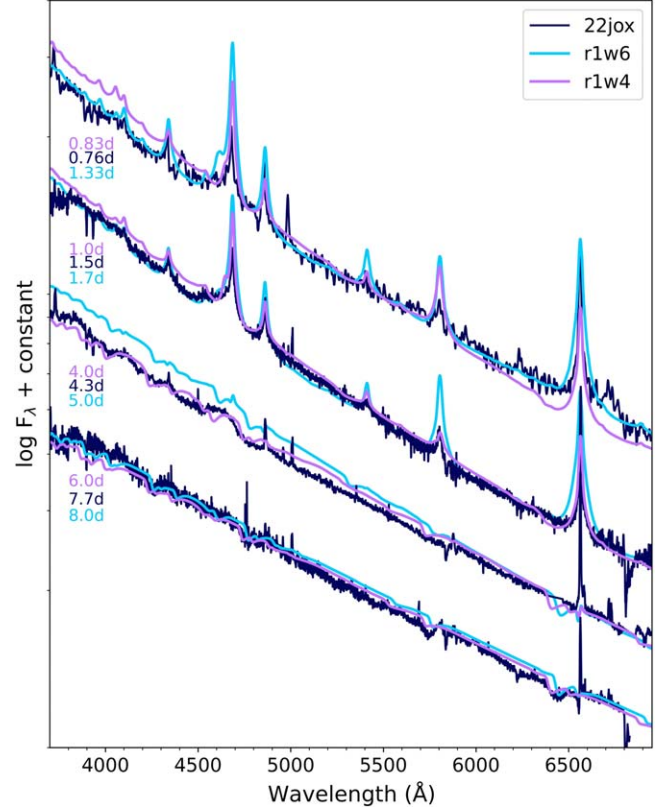


Figure 14. Comparison of the early optical spectra of SN 2022jox to the $r1w4$ and $r1w6$ models of Dessart et al. (2017). These models have a mass-loss rate of $10^{-3} M_\odot \text{ yr}^{-1}$ and $10^{-2} M_\odot \text{ yr}^{-1}$, respectively.

models $r1w6$ and $r1w4$, which have an $\dot{M} = 10^{-2} M_\odot \text{ yr}^{-1}$ and $\dot{M} = 10^{-3} M_\odot \text{ yr}^{-1}$, respectively. The comparisons are shown in Figure 14.

One caveat is that there is a varying cadence and sampling available for each model, with $r1w4$ starting at 0.83 day and $r1w6$ at 1.33 days, so a perfect temporal match is not always possible. Regardless, there are similarities between both models and the optical spectra of SN 2022jox that indicate a high degree of mass loss from the progenitor. For example, the 1.5 days spectrum of SN 2022jox is matched almost perfectly on the blue end of the 1.7 days spectrum from the $r1w6$ model, but the $\text{H}\alpha$ and C IV shape and strength is very well matched by the $r1w4$ 1 day model. The 4.3 days spectrum of SN 2022jox shows the opposite, with the slope of the continuum and the broad, ledge-shaped feature around 4600 \AA discussed in detail above being fit better by the 4.0 days spectrum from the $r1w4$ model. There is also stronger $\text{H}\alpha$ emission in the spectrum of SN 2022jox at this epoch, but based on the strength of other H II region lines in the spectrum this is likely not associated with the SN. Both models also show narrow $\text{N III } \lambda 4636$ at early times with various intensities, something which we do not see (or failed to catch) in SN 2022jox. Finally, our mostly featureless day 7.7 spectrum is well represented by both the 6 days $r1w4$ model (there is no 8 days $r1w4$ model) and the 8 days $r1w6$ model, including continuum shape and the start of the emergence of a broad, blueshifted $\text{H}\alpha$.

Additionally, if we compare the early light curves from the Dessart et al. (2017) models to our data, we also see that while the shapes may not match perfectly, the absolute magnitudes are consistent with both $r1w4$ and $r1w6$ models (Figure 15).

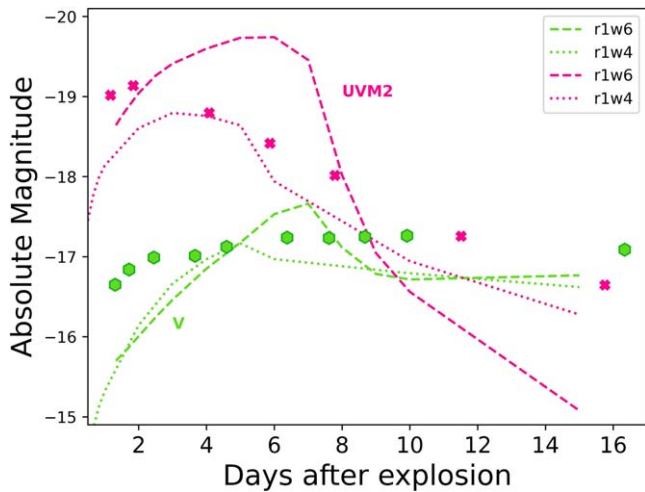


Figure 15. Comparison of the early V -band and $UVW2$ SN 2022jox light curves compared with the light curves generated from the $r1w4$ and $r1w6$ models of Dessart et al. (2017). These models have a mass-loss rate of $10^{-3} M_{\odot} \text{ yr}^{-1}$ and $10^{-2} M_{\odot} \text{ yr}^{-1}$, respectively.

From the similarities between the spectra and the models as well as the fits of the light curves to the shock-cooling models above, we are fairly confident in concluding that the progenitor of SN 2022jox was likely an RSG with a radius of $\sim 600\text{--}700 R_{\odot}$ that experienced a rather strong mass-loss rate of $\dot{M} = 10^{-3} - 10^{-2} M_{\odot} \text{ yr}^{-1}$.

5.2. The Progenitor Mass-loss Rate

When combining the model fits and the comparison to other similar SNe, such as SN 2014G and SN 2023ixf, we seem to reach a consensus of a high mass-loss rate being responsible for the early spectroscopic and photometric evolution of SN 2022jox. In particular, direct comparison between SN 2022jox and SN 2023ixf can be useful. Using similar techniques as done here, Hosseinzadeh et al. (2023b) found a progenitor radius of $410 \pm 10 R_{\odot}$ for SN 2023ixf, smaller than the radius of SN 2022jox. The faster spectral evolution of SN 2022jox out of the flash stage does suggest a less extended, dense CSM, possibly along with some combination of underestimating the explosion epoch. This is also consistent with the model fitting of the early SN 2023ixf spectra suggesting a larger \dot{M} , and a longer period of flash features (Bostroem et al. 2023; Jacobson-Galán et al. 2023), as well as the absence of narrow N III/C III in SN 2022jox. This is, of course, assuming both SNe have a symmetric CSM, which may not be the case for SN 2023ixf (Li et al. 2023; Smith et al. 2023) or possibly SN 2022jox, as mentioned in Section 4 above.

While stellar evolutionary models are still not robust for evolved massive stars, in order to have such high \dot{M} values, mechanisms other than steady winds are likely at play in the end point of RSG evolution. For instance, recently revised studies of \dot{M} from observed RSGs find that even the most luminous members seem to have quiescent mass losses of at maximum $\dot{M} \sim 10^{-5} M_{\odot} \text{ yr}^{-1}$ (Beasor et al. 2020). As an example, in SN 2023ixf from the analysis of the early spectra the mass-loss rate was estimated to be $\dot{M} = 10^{-3} - 10^{-2} M_{\odot} \text{ yr}^{-1}$ (Bostroem et al. 2023; Hiramatsu et al. 2023; Jacobson-Galán et al. 2023; Zhang et al. 2023), while values derived from the progenitor RSG suggests $\dot{M} = 10^{-5} - 10^{-4} M_{\odot} \text{ yr}^{-1}$ (Jencson et al. 2023;

Kilpatrick et al. 2023; Xiang et al. 2024). Therefore, a period of enhanced mass loss from a superwind phase, a sudden outburst, or a binary companion in the weeks to years before explosion may need to be invoked, particularly for the class of objects showing flash ionization. This phase may be short lived, making it very difficult to observe in RSG populations. Unfortunately, no pre-explosion imaging is available for the progenitor of SN 2022jox to allow for a direct comparison.

6. Conclusions

We have presented a comprehensive optical and UV light curve and spectral sequence for the normal Type II SN 2022jox, which was observed within the first day of estimated explosion, giving us a rare chance to observe the early-time spectral evolution. Other than the dense, nearby CSM surrounding the SN giving rise to flash features in the optical spectra, the evolution of the object is quite normal for Type II SNe. Had it been discovered a few days later, it may have appeared as a generic Type II SN.

The early-time spectra show lines of H I, He II, C IV, and N IV, but lack C III, N III, and O IV. These lines last up to at least ~ 5 days, after which broad Balmer and other common Type II SN emission lines emerge. SN 2022jox has a V -band light curve with a ~ 10 day rise to maximum, an almost linear decline over the next few weeks, followed by a more steady plateau starting at day 50 until the SN becomes Sun constrained. The late-time radioactive tail follows ^{56}Co decay, and suggests a rather average ^{56}Ni mass of $0.04 M_{\odot}$. There is also multicomponent H α emission at late times, possibly from interaction with asymmetric CSM, although deep, late-time spectra are needed to confirm this.

By modeling the early light-curve evolution with shock-cooling models, we find a best-fit radius of $R = 600\text{--}700 R_{\odot}$ (although the presence of CSM complicates this calculation), making it highly likely that the progenitor was a RSG. Using radiative-transfer models to compare against early spectra of SN 2022jox indicates that the progenitor went through a period of enhanced mass loss of $\dot{M} = 10^{-3} - 10^{-2} M_{\odot} \text{ yr}^{-1}$ in the years before explosion.

SN 2022jox is an example of a Type II SN that shows both early- and late-time signatures of CSM interaction through flash spectroscopy in early spectra and multicomponent H α emission in the nebular spectra. This adds to the increasing evidence that the extent and percentage of “normal” Type II SNe having CSM interaction is likely quite a lot higher than once believed, and that early and long-term monitoring of these objects are needed to fully understand the late-time evolution of massive stars.

Acknowledgments

We thank the anonymous referee for the helpful comments on this manuscript. We also thank Luc Dessart for providing his model spectra. Based on observations obtained at the international Gemini Observatory (GN-2022A-Q-135 and GS-2022A-Q-145; PI: Andrews), a program of NSF’s NOIRLab, which is managed by the Association of Universities for Research in Astronomy (AURA) under a cooperative agreement with the National Science Foundation. On behalf of the Gemini Observatory partnership: the National Science Foundation (United States), National Research Council (Canada), Agencia Nacional de Investigación y Desarrollo (Chile),

Ministerio de Ciencia, Tecnología e Innovación (Argentina), Ministério da Ciência, Tecnologia, Inovações e Comunicações (Brazil), and Korea Astronomy and Space Science Institute (Republic of Korea). This work was enabled by observations made from the Gemini North telescope, located within the Maunakea Science Reserve and adjacent to the summit of Maunakea. We are grateful for the privilege of observing the Universe from a place that is unique in both its astronomical quality and its cultural significance.

The SALT spectra presented here were obtained through the Rutgers University SALT program 2022-1-MLT-004 (PI: Jha). Based in part on observations obtained at the Southern Astrophysical Research (SOAR) telescope, which is a joint project of the Ministério da Ciência, Tecnologia e Inovações (MCTI/LNA) do Brasil, the US National Science Foundation's NOIRLab, the University of North Carolina at Chapel Hill (UNC), and Michigan State University (MSU).

Time-domain research by the University of Arizona team and D.J.S. is supported by NSF grants AST-1821987, 1813466, 1908972, 2108032, and 2308181, and by the Heising-Simons Foundation under grant No. 2020-1864. The research by Y.D., S.V., N.M., and E.H. is supported by NSF grant AST-2008108. The LCO team is supported by NSF grants AST-1911225 and AST-1911151, and NASA Swift grant No. 80NSSC19K1639.

Research by Y.D., S.V., N.M.R., and E.H. is supported by NSF grant AST-2008108. K.A.B. is supported by an LSSTC Catalyst Fellowship; this publication was thus made possible through the support of Grant 62192 from the John Templeton Foundation to LSSTC. The opinions expressed in this publication are those of the authors and do not necessarily reflect the views of LSSTC or the John Templeton Foundation. This work makes use of data taken with the Las Cumbres Observatory global telescope network. The LCO group is supported by NSF grants 1911225 and 1911151.

This research has made use of the NASA Astrophysics Data System (ADS) Bibliographic Services, and the NASA/IPAC Infrared Science Archive (IRSA), which is funded by the National Aeronautics and Space Administration and operated by the California Institute of Technology. This work made use of data supplied by the UK Swift Science Data Centre at the University of Leicester.

Facilities: NED, Gemini:Gillett, Gemini:South, SALT, SOAR, LCOGT, FTN, FTS, CTIO:PROMPT.

Software: astropy (Astropy Collaboration et al. 2013, 2018), Cloudy (Ferland et al. 2013), Source Extractor (Bertin & Arnouts 1996), DRAGONS (Labrie et al. 2019).

ORCID iDs

Jennifer E. Andrews <https://orcid.org/0000-0003-0123-0062>

Jeniveve Pearson <https://orcid.org/0000-0002-0744-0047>

Griffin Hosseinzadeh <https://orcid.org/0000-0002-0832-2974>

K. Azalee Bostroem <https://orcid.org/0000-0002-4924-444X>

Yize Dong (董一泽) <https://orcid.org/0000-0002-7937-6371>

Manisha Shrestha <https://orcid.org/0000-0002-4022-1874>

Jacob E. Jencson <https://orcid.org/0000-0001-5754-4007>

David J. Sand <https://orcid.org/0000-0003-4102-380X>

S. Valenti <https://orcid.org/0000-0001-8818-0795>

Emily Hoang <https://orcid.org/0000-0003-2744-4755>
 Daryl Janzen <https://orcid.org/0000-0003-0549-3281>
 M. J. Lundquist <https://orcid.org/0000-0001-9589-3793>
 Nicolás Meza <https://orcid.org/0000-0002-7015-3446>
 Samuel Wyatt <https://orcid.org/0000-0003-2732-4956>
 Saurabh W. Jha <https://orcid.org/0000-0001-8738-6011>
 Chris Simpson <https://orcid.org/0000-0001-8589-4055>
 Joseph Farah <https://orcid.org/0000-0003-4914-5625>
 Estefania Padilla Gonzalez <https://orcid.org/0000-0003-0209-9246>
 D. Andrew Howell <https://orcid.org/0000-0003-4253-656X>
 Curtis McCully <https://orcid.org/0000-0001-5807-7893>
 Megan Newsome <https://orcid.org/0000-0001-9570-0584>
 Craig Pellegrino <https://orcid.org/0000-0002-7472-1279>
 Giacomo Terran <https://orcid.org/0000-0003-0794-5982>

References

Anderson, J. P. 2019, *A&A*, **628**, A7
 Anderson, J. P., Dessart, L., Gutierrez, C. P., et al. 2014a, *MNRAS*, **441**, 671
 Anderson, J. P., González-Gaitán, S., Hamuy, M., et al. 2014b, *ApJ*, **786**, 67
 Andrews, J. E., Gallagher, J. S., Clayton, G. C., et al. 2010, *ApJ*, **715**, 541
 Andrews, J. E., Sand, D. J., Valenti, S., et al. 2019, *ApJ*, **885**, 43
 Arcavi, I. 2017, in *Handbook of Supernovae*, ed. A. W. Alsabti & P. Murdin (New York: Springer), 239
 Astropy Collaboration, Price-Whelan, A. M., Sipőcz, B. M., et al. 2018, *AJ*, **156**, 123
 Astropy Collaboration, Robitaille, T. P., Tollerud, E. J., et al. 2013, *A&A*, **558**, A33
 Barbon, R., Ciatti, F., & Rosino, L. 1979, *A&A*, **72**, 287
 Beasor, E. R., Davies, B., Smith, N., et al. 2020, *MNRAS*, **492**, 5994
 Benetti, S., Patat, F., Turatto, M., et al. 1994, *A&A*, **285**, L13
 Bertin, E., & Arnouts, S. 1996, *A&AS*, **117**, 393
 Bose, S., Valenti, S., Misra, K., et al. 2015, *MNRAS*, **450**, 2373
 Bostroem, K. A., Jencson, J., Janzen, D., et al. 2022, *Transient Name Server Discovery Report*, TNS, **2022-150**
 Bostroem, K. A., Pearson, J., Shrestha, M., et al. 2023, *ApL*, **956**, L5
 Bradley, L., Sipőcz, B., Robitaille, T., et al. 2022, *astropy/photutils*: 1.6.0, v1.6.0, Zenodo, doi:[10.5281/zenodo.7419741](https://doi.org/10.5281/zenodo.7419741)
 Branch, D., & Wheeler, J. C. 2017, *Supernova Explosions* (Berlin: Springer)
 Brown, T. M., Baliber, N., Bianco, F. B., et al. 2013, *PASP*, **125**, 1031
 Bruch, R. J., Gal-Yam, A., Schulze, S., et al. 2021, *ApJ*, **912**, 46
 Bruch, R. J., Gal-Yam, A., Yaron, O., et al. 2023, *ApJ*, **952**, 119
 Bullivant, C., Smith, N., Williams, G. G., et al. 2018, *MNRAS*, **476**, 1497
 Clemens, J. C., Crain, J. A., & Anderson, R. 2004, *Proc. SPIE*, **5492**, 331
 Crawford, S. M., Still, M., Schellart, P., et al. 2010, *Proc. SPIE*, **7737**, 773725
 Davies, B., & Dessart, L. 2019, *MNRAS*, **483**, 887
 Davies, B., Plez, B., & Petrault, M. 2022, *MNRAS*, **517**, 1483
 de Jager, C., Nieuwenhuijzen, H., & van der Hucht, K. A. 1988, *A&AS*, **72**, 259
 Dessart, L., Gutierrez, C. P., Kuncarayakti, H., Fox, O. D., & Filippenko, A. V. 2023, *A&A*, **675**, A33
 Dessart, L., & Hillier, D. J. 2005, *A&A*, **439**, 671
 Dessart, L., Hillier, D. J., & Audit, E. 2017, *A&A*, **605**, A83
 Dong, Y., Sand, D. J., Valenti, S., et al. 2023, *ApJ*, **957**, 28
 Ekström, S., Georgy, C., Eggenberger, P., et al. 2012, *A&A*, **537**, A146
 Ferland, G. J., Porter, R. L., van Hoof, P. A. M., et al. 2013, *RMxAA*, **49**, 137
 Fransson, C., Challis, P. M., Chevalier, R. A., et al. 2005, *ApJ*, **622**, 991
 Fuller, J. 2017, *MNRAS*, **470**, 1642
 Gal-Yam, A. 2017, in *Handbook of Supernovae*, ed. A. W. Alsabti & P. Murdin (New York: Springer), 195
 Gal-Yam, A., Arcavi, I., Ofek, E. O., et al. 2014, *Natur*, **509**, 471
 Gal-Yam, A., Kasliwal, M. M., Arcavi, I., et al. 2011, *ApJ*, **736**, 159
 Gehrels, N., Chincarini, G., Giommi, P., et al. 2004, *ApJ*, **611**, 1005
 Gimeno, G., Roth, K., Chiboucas, K., et al. 2016, *Proc. SPIE*, **9908**, 99082S
 González-Gaitán, S., Tominaga, N., Molina, J., et al. 2015, *MNRAS*, **451**, 2212
 Groh, J. H., Meynet, G., Ekström, S., & Georgy, C. 2014, *A&A*, **564**, A30
 Hamuy, M. 2003, *ApJ*, **582**, 905
 Henden, A. A., Welch, D. L., Terrell, D., & Levine, S. E. 2009, *AAS Meeting*, **214**, 407.02
 Hirayama, D., Howell, D. A., Moriya, T. J., et al. 2021, *ApJ*, **913**, 55
 Hirayama, D., Tsuna, D., Berger, E., et al. 2023, *ApJL*, **955**, L8

Hook, I. M., Jørgensen, I., Allington-Smith, J. R., et al. 2004, *PASP*, **116**, 425

Hosseinzadeh, G., Bostroem, K. A., & Gomez, S. 2023a, Light Curve Fitting, v0.8.0, Zenodo, doi:[10.5281/zenodo.7872772](https://doi.org/10.5281/zenodo.7872772)

Hosseinzadeh, G., Farah, J., Shrestha, M., et al. 2023b, *ApJL*, **953**, L16

Hosseinzadeh, G., Kilpatrick, C. D., Dong, Y., et al. 2022, *ApJ*, **935**, 31

Hosseinzadeh, G., Valenti, S., McCully, C., et al. 2018, *ApJ*, **861**, 63

Jacobson-Galán, W. V., Dessart, L., Jones, D. O., et al. 2022, *ApJ*, **924**, 15

Jacobson-Galán, W. V., Dessart, L., Margutti, R., et al. 2023, *ApJL*, **954**, L42

Jencson, J. E., Pearson, J., Beasor, E. R., et al. 2023, *ApJL*, **952**, L30

Jerkstrand, A., Fransson, C., Maguire, K., et al. 2012, *A&A*, **546**, A28

Khazov, D., Yaron, O., Gal-Yam, A., et al. 2016, *ApJ*, **818**, 3

Kilpatrick, C. D., Foley, R. J., Jacobson-Galán, W. V., et al. 2023, *ApJL*, **952**, L23

Kochanek, C. S., Fraser, M., Adams, S. M., et al. 2017, *MNRAS*, **467**, 3347

Kregel, M., van der Kruit, P. C., & de Blok, W. J. G. 2004, *MNRAS*, **352**, 768

Labrie, K., Anderson, K., Cárdenes, R., Simpson, C., & Turner, J. E. H. 2019, in *ASP Conf. Ser. Vol. 523, Astronomical Data Analysis Software and Systems XXVII*, ed. P. J. Teuben et al. (San Francisco, CA: ASP), 321

Leonard, D. C., Filippenko, A. V., Barth, A. J., & Matheson, T. 2000, *ApJ*, **536**, 239

Li, G., Hu, M., Li, W., et al. 2023, arXiv:[2311.14409](https://arxiv.org/abs/2311.14409)

Mauerhan, J., & Smith, N. 2012, *MNRAS*, **424**, 2659

Morag, J., Sapir, N., & Waxman, E. 2023, *MNRAS*, **522**, 2764

Moran, S., Fraser, M., Kotak, R., et al. 2023, *A&A*, **669**, A51

Morozova, V., Piro, A. L., & Valenti, S. 2017, *ApJ*, **838**, 28

Morozova, V., Piro, A. L., & Valenti, S. 2018, *ApJ*, **858**, 15

Müller, T., Prieto, J. L., Pejcha, O., & Clocchiatti, A. 2017, *ApJ*, **841**, 127

Nakaoka, T., Kawabata, K. S., Maeda, K., et al. 2018, *ApJ*, **859**, 78

Niemela, V. S., Ruiz, M. T., & Phillips, M. M. 1985, *ApJ*, **289**, 52

Pastorello, A., Sauer, D., Taubenberger, S., et al. 2006, *MNRAS*, **370**, 1752

Pearson, J., Hosseinzadeh, G., Sand, D. J., et al. 2023, *ApJ*, **945**, 107

Pejcha, O., & Prieto, J. L. 2015, *ApJ*, **799**, 215

Poznanski, D., Prochaska, J. X., & Bloom, J. S. 2012, *MNRAS*, **426**, 1465

Pritchard, T. A., Roming, P. W. A., Brown, P. J., Bayless, A. J., & Frey, L. H. 2014, *ApJ*, **787**, 157

Quataert, E., & Shiode, J. 2012, *MNRAS*, **423**, L92

Quimby, R. M., Wheeler, J. C., Höflich, P., et al. 2007, *ApJ*, **666**, 1093

Reichart, D., Nysewander, M., Moran, J., et al. 2005, *NCimC*, **28**, 767

Rodríguez, Ó., Meza, N., Pineda-García, J., & Ramirez, M. 2021, *MNRAS*, **505**, 1742

Roming, P. W. A., Kennedy, T. E., Mason, K. O., et al. 2005, *SSRv*, **120**, 95

Rubin, A., Gal-Yam, A., De Cia, A., et al. 2016, *ApJ*, **820**, 33

Sana, H., de Mink, S. E., de Koter, A., et al. 2012, *Sci*, **337**, 444

Sapir, N., & Waxman, E. 2017, *ApJ*, **838**, 130

Schlafly, E. F., & Finkbeiner, D. P. 2011, *ApJ*, **737**, 103

SDSS Collaboration, Albareti, F. D., Allende Prieto, C., et al. 2017, *ApJS*, **233**, 25

Shrestha, M., Pearson, J., Wyatt, S., et al. 2024, *ApJ*, **961**, 247

Smartt, S. J. 2015, *PASA*, **32**, e016

Smith, K. W., Smartt, S. J., Young, D. R., et al. 2020, *PASP*, **132**, 085002

Smith, M. P., Nordsieck, K. H., Burgh, E. B., et al. 2006, *Proc. SPIE*, **6269**, 62692A

Smith, N. 2014, *ARA&A*, **52**, 487

Smith, N., & Arnett, W. D. 2014, *ApJ*, **785**, 82

Smith, N., Mauerhan, J. C., Cenko, S. B., et al. 2015, *MNRAS*, **449**, 1876

Smith, N., Pearson, J., Sand, D. J., et al. 2023, *ApJ*, **956**, 46

Smith, N., Silverman, J. M., Chornock, R., et al. 2009, *ApJ*, **695**, 1334

Soumagnac, M. T., Ganot, N., Irani, I., et al. 2020, *ApJ*, **902**, 6

Stetson, P. B. 2000, *PASP*, **112**, 925

Szalai, T., Vinkó, J., Könyves-Tóth, R., et al. 2019, *ApJ*, **876**, 19

Tartaglia, L., Sand, D. J., Groh, J. H., et al. 2021, *ApJ*, **907**, 52

Tartaglia, L., Sand, D. J., Valenti, S., et al. 2018, *ApJ*, **853**, 62

Terreran, G., Jacobson-Galán, W. V., Groh, J. H., et al. 2022, *ApJ*, **926**, 20

Terreran, G., Jerkstrand, A., Benetti, S., et al. 2016, *MNRAS*, **462**, 137

Tonry, J. L., Denneau, L., Heinze, A. N., et al. 2018, *PASP*, **130**, 064505

Tsuna, D., Takei, Y., & Shigeyama, T. 2023, *ApJ*, **945**, 104

Tully, R. B., Courtois, H. M., & Sorce, J. G. 2016, *AJ*, **152**, 50

Valenti, S., Andrews, J. E., Lundquist, M., et al. 2022, Transient Name Server Classification Report, TNS, [2022-1232](https://tns.berkeley.edu/classification/2022-1232)

Valenti, S., Howell, D. A., Stritzinger, M. D., et al. 2016, *MNRAS*, **459**, 3939

Valenti, S., Sand, D., Pastorello, A., et al. 2014, *MNRAS*, **438**, L101

Van Dyk, S. D. 2015, *IAUGA*, **29**, 2256013

Woosley, S. E., Pinto, P. A., & Hartmann, D. 1989, *ApJ*, **346**, 395

Wu, S., & Fuller, J. 2021, *ApJ*, **906**, 3

Xiang, D., Mo, J., Wang, L., et al. 2024, *SCPMA*, **67**, 219514

Yaron, O., Perley, D. A., Gal-Yam, A., et al. 2017, *NatPh*, **13**, 510

Zhang, J., Lin, H., Wang, X., et al. 2023, arXiv:[2309.01998](https://arxiv.org/abs/2309.01998)